Progress In Electromagnetics Research, Vol. 157, 93–110, 2016

Optimal Illumination Schemes for Near-Field Microwave Imaging

Denys S. Shumakov*, Alexander S. Beaverstone, and Natalia K. Nikolova

Abstract—Axial-null illumination (ANI) is proposed to simplify the calibration of microwave imaging systems. The illumination also enhances the spatial resolution. ANI can be achieved with various array configurations, but a minimum of two transmitting antennas are required, which is a well-known form of differential illumination. Here, ANI is achieved with four transmitting antennas, and its implementation is investigated in a planar scanning scenario. The receiving antenna resides at the radiation null of the ANI array. Back-scattered reception requires an antenna at the center of the ANI array whereas forward-scattered reception requires an antenna aligned with the ANI axis, but on the opposite side of the imaged volume. The most important advantage of the proposed imaging setup is that it eliminates the need for background (or baseline) measurements, thus simplifying the system calibration. Also, it is proven that at least two-fold improvement in the spatial resolution can be achieved in near-field imaging scenarios compared to the conventional single-source illumination.

1. INTRODUCTION

Recent efforts in microwave imaging target a variety of short-range applications such as concealed weapon detection, through-the-wall imaging, non-destructive testing and evaluation, biomedical diagnostics, etc. [1–6]. The scanning hardware usually employs acquisition surfaces of canonical shapes: planar, cylindrical, or hemispherical, which simplifies the reconstruction process. The data (back-scattered and/or forward-scattered signals) can be acquired either through mechanical scanning or through electronically-switched arrays. The transmitting antennas are designed to conform to the respective surface shape and to have the radiation maximum more or less along boresight and aiming at the center of the examined volume. This design choice achieves stronger scattering signals from possible targets — the stronger the illumination is, the stronger the scattered field. Further, in forward-scattered (transmission coefficient) data acquisition, it is customary to align at least one of the receiving antennas (the sensors) along the transmitters' boresight in order to minimize the signal path, thereby maximizing the signal strength. In back-scattered (reflection coefficient) data acquisition, it is customary to use the same antenna as a transmitter and a receiver along with a duplexing device that separates the incoming (reflected) signal from the outgoing (transmitted) one.

Multi-illumination configurations, also known as illumination-diversity techniques, have been used widely in microwave imaging [7–15]. At the expense of increased hardware complexity, such configurations allow for more accurate target shape reconstruction and localization. This is a consequence of collecting data from multiple perspectives. Illumination diversity along with frequency diversity can drastically improve the performance of microwave imaging provided the design of the system is optimal.

It is known that multi-illumination data improve the spatial resolution [8–15]. Since the object under test (OUT) is simultaneously illuminated by multiple sources, the scattered signals produce a coherent summation of the field due to a scattering center. For example, in diffraction tomography,

Received 8 July 2016, Accepted 27 October 2016, Scheduled 4 November 2016
* Corresponding author: Denys S. Shumakov (shumakds@mcmaster.ca).
The authors are with the Department of Electrical and Computer Engineering, McMaster University, Hamilton, Canada.

this improves the image angular resolution, which is equivalent to reducing the necessary rotation angles [8, 9]. In the quasi-monostatic frequency-swept imaging system in [8], three transmitting antennas are used, the boresight axes of which are at 0°, 30° and −30° angles with respect to the radial line through the center of the imaged plane. At the same time, the receiving antenna boresight is at an angle of 0°. This leads to three-fold improvement in the spatial resolution compared to a single-source illumination using the same angular sampling rate.

Microwave multi-static tomography systems such as [11–15] can also achieve improvement in resolution due to the multiple viewing angles. Such systems employ circular switched arrays where, at each measurement, one antenna transmits, and all others receive. However, due to reciprocity, the acquired signals can also be interpreted as due to multiple transmitters with a single receiver. Similarly, the reciprocity concept has been exploited in the ultrawideband (UWB) radar systems such as that in [10], where only one antenna transmits and 24 antennas receive back-scattered signals. A major advantage of the radar-based imaging over the tomographic imaging is its relatively simple and robust signal processing [16]. Some examples of the multistatic UWB radar microwave imaging systems are presented in [17] and [18]. They employ 31 antennas which can operate as transmitters or as receivers: while one antenna transmits, the measured field is acquired by the remaining 30 antennas.

Finally, the different strategies can be combined in order to achieve an improved resolution. These strategies can be algorithmic such as multi-resolution iterative inversion or edge preserving regularization, and hardware-oriented such as multi-illumination or multi-frequency excitation. For example, a multi-illumination setup used in conjunction with the multi-resolution iterative inversion is discussed in [19–21].

This paper starts with the presentation of a rigorous theory of the spatial resolution for the case of multi-illumination schemes. The cross-range resolution limits with planar scanning are derived analytically in the far zone allowing for a comparison between the conventional single-source illumination and the double-source illumination. These limits are then validated through inversion with the direct reconstruction method proposed in [22], referred to as scattered-power mapping (SPM). This method is fast (quasi-real time), easy to implement and accurate within the limits of the linear Born approximation. The reconstruction is applied to two sets of simulated data acquired by a four-antenna array and by the conventional illumination. The respective images provide the estimated resolution limits in both cases. Next, the axial-null illumination for near-field microwave imaging is introduced. In addition to the improved cross-range resolution, the important advantage of the proposed illumination scheme is that it eliminates the need for background (or baseline) measurements, thus simplifying the system calibration.

2. ANALYTICAL INVESTIGATION OF SPATIAL RESOLUTION LIMITS

2.1. Cross-Range Resolution

To estimate the cross-range resolution limit, consider the planar scanning scenario depicted in Fig. 1. The scan is along x and y whereas z is the depth (or range) direction. It is assumed that the scatterer lies in a fixed cross-range plane $z = z_0$ where its contrast function is given by $f(x', y', z_0)$. Under the linear Born approximation, a signal in a planar acquisition can be viewed as the 2D convolution of the contrast function and the point-spread function (PSF) of the measurement system S_0 [23]:

$$S(x, y, z_A) = \int_{x'} \int_{y'} f(x', y', z_0) \cdot S_0(x - x', y - y', z_0)\, dx' dy', \tag{1}$$

where z_A is the fixed z-coordinate of the acquisition plane whereas x and y indicate the location of the measurement point. $S_0(x, y, z_0)$ is a short-hand notation for

$$S_0(x, y, z_0) \equiv S_\delta(x, y, z_A; 0, 0, z_0) \tag{2}$$

and it describes the system's centered PSF, i.e., the signal recorded at (x, y, z_A), when a point (δ-function) scatterer is located at the center $(0, 0, z_0)$ of the imaged plane. The subscript in S_δ emphasizes that this signal is due to a point scatterer.

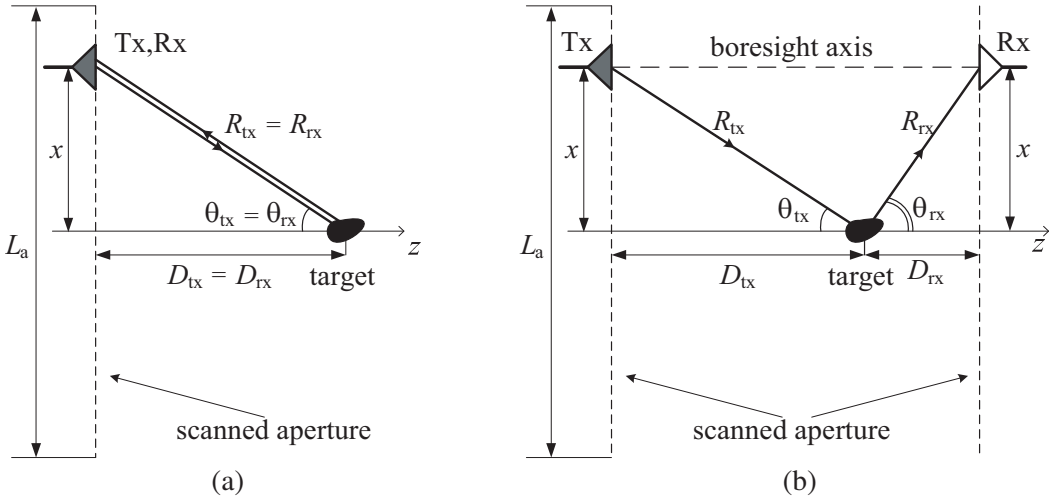

Figure 1. Illustration of the antenna and target positions in planar raster scanning in the case of conventional single antenna illumination: (a) monostatic, (b) bi-static.

In Fourier (or k) space, Eq. (1) can be written as

$$\tilde{S}(k_x, k_y, z_A) = \tilde{f}(k_x, k_y, z_0) \cdot \tilde{S}_0(k_x, k_y, z_0), \tag{3}$$

which allows for expressing the 2D Fourier transform (FT) of the unknown contrast function as

$$\tilde{f}(k_x, k_y, z_0) = \frac{\tilde{S}(k_x, k_y, z_A)}{\tilde{S}_0(k_x, k_y, z_0)}. \tag{4}$$

Here, $\tilde{S}$ and $\tilde{S}_0$ denote the 2D FT of S and S_0, respectively. It should be noted that (4) is not used directly in practical inversion schemes because $\tilde{S}_0(k_x, k_y, z_0)$ may have near-zero values, or a system of equations based on Eq. (3) may be ill-posed and/or over-determined. Here, Eq. (4) is used only to illustrate the impact of the limits of the signal extent in k-space on the spatial resolution and to estimate the limits of this resolution.

Assuming that Eq. (4) is valid, the contrast function can be reconstructed using

$$\widehat{f}(x, y, z_0) = \mathcal{F}_{2D}^{-1} \left\{ \frac{\tilde{S}(k_x, k_y, z_A)}{\tilde{S}_0(k_x, k_y, z_0)} \right\}, \tag{5}$$

where $\mathcal{F}_{2D}^{-1}$ denotes the 2D inverse FT, and $\widehat{f}$ is the estimate of f.

Consider a point scatterer at (x_0, y_0) in the z_0 plane. Its contrast function is defined as

$$f_\delta(x, y) = \delta(x - x_0)\delta(y - y_0). \tag{6}$$

In 2D k-space, this scatterer appears as

$$\tilde{f}_\delta(k_x, k_y, z_0) = e^{-jk_x x_0 - jk_y y_0}. \tag{7}$$

From Eq. (3), the FT of the system PSF is obtained as

$$\tilde{S}_\delta(k_x, k_y, z_A) = e^{-jk_x x_0 - jk_y y_0} \cdot \tilde{S}_0(k_x, k_y, z_0). \tag{8}$$

Substituting Eq. (8) into Eq. (5) produces the reconstructed contrast function, which is in the form of a 2D *sinc* function (centered at x_0, y_0) due to the finite spectral range limited between $-k_\xi^{\max}$ and $+k_\xi^{\max}$, $\xi = x, y$. These limits depend on the spectral content of $\tilde{S}_0$, which in turn depends on the size of the scanned aperture as well as the transmitting and receiving antenna radiation patterns. The first null of the *sinc* function, which estimates the actual δ-function contrast, determines the cross-range resolution limits as:

$$\delta_x = \frac{\pi}{k_x^{\max}}, \quad \delta_y = \frac{\pi}{k_y^{\max}}. \tag{9}$$

Thus, the available spectral width in k-space is critical in improving the cross-range resolution. Also, note that Eq. (5) is an approximation that yields the best possible resolution for the given spectral limits. As the scatterer moves from the center of the imaged scene and toward the edge of the acquisition aperture, the cross-range resolution will deteriorate.

2.1.1. Conventional Boresight Illumination

In order to compare the spectral width of the signals acquired with the conventional boresight illumination and those acquired with ANI, it is beneficial to analyze the simplified problem of a linear scan along the x-axis where the target is in the far zone of the transmitting (Tx) and the receiving (Rx) antennas. Let x be the position of the Tx/Rx antenna pair with respect to the target (see Fig. 1). The faster the acquired signal $S(x)$ changes with x, the broader its spectrum is in k_x space. Thus, increasing the sensitivity of the signal dS/dx is equal to increasing the spectral width $k_x^{\max}$, which in turn means better resolution.

As discussed before, the available spectral range in Fourier space is determined by that of the system PSF, $S_0(x, z_0)$, which is the signal acquired at x when a point scatterer is located at $(x_0 = 0, z_0)$; see Eq. (2). Let z_0 be such that the range distances from the scatterer to the planes of the transmitter and the receiver are $D_{\rm tx}$ and $D_{\rm rx}$, respectively; see Fig. 1. For simplicity, we consider the scenario where the receiving and transmitting antennas are co-located (see the monostatic-case illustration in Fig. 1(a)) or they are on the opposite sides of the target but scan together the x-line while remaining aligned along each other's boresight (see the bistatic-case illustration in Fig. 1(b)). The scanned aperture has length $L_{\rm a}$ so that $x \in [-0.5L_{\rm a}, 0.5L_{\rm a}]$.

The far-zone assumption allows for neglecting the amplitude variation of the received signal, so that

$$S_0(x) \approx S_{\rm a}(x) = e^{-jk(R_{\rm tx}+R_{\rm rx})}. \tag{10}$$

Here, $R_{\rm tx}(x) = \sqrt{D_{\rm tx}^2 + x^2}$ and $R_{\rm rx}(x) = \sqrt{D_{\rm rx}^2 + x^2}$. The subscript in $S_{\rm a}$ emphasizes that the expression is only approximate. The signal derivative with respect to x is found as

$$\frac{dS_{\rm a}}{dx} = -jk(\sin\theta_{\rm tx} + \sin\theta_{\rm rx}) \cdot S_{\rm a}(x), \tag{11}$$

where $\sin\theta_{\rm tx} = x/R_{\rm tx}$ and $\sin\theta_{\rm rx} = x/R_{\rm rx}$. It is apparent that the maximum derivative occurs at the largest values of $\theta_{\rm tx}$ and $\theta_{\rm rx}$, i.e., when the antennas are at the edge of the aperture:

$$\sin\theta_{\rm tx}^{\max} = \frac{L_{\rm a}}{2R_{\rm tx}}; \quad \sin\theta_{\rm rx}^{\max} = \frac{L_{\rm a}}{2R_{\rm rx}}. \tag{12}$$

Therefore, the signals acquired at the aperture's edge contribute to the highest spectral content of $\tilde{S}_0(k_x)$. The spatial frequencies of this content can be estimated by taking the Fourier transform of Eq. (11), where $\sin\theta_{\rm tx}$ and $\sin\theta_{\rm rx}$ are assumed relatively constant (with respect to x) close to their maximum values. This yields the estimate of the maximum spatial frequency as

$$|k_x^{\max}| \approx k(\sin\theta_{\rm tx}^{\max} + \sin\theta_{\rm rx}^{\max}). \tag{13}$$

In the best case scenario, $\theta_{\rm tx}^{\max} \to 90^\circ$ and $\theta_{\rm rx}^{\max} \to 90^\circ$. Then, $|k_x^{\max}| \approx 2k$ and, according to Eq. (9),

$$\delta_x = \frac{\pi}{|k_x^{\max}|} \approx \frac{\lambda}{4}. \tag{14}$$

This is the well-known diffraction limit of imaging with far-zone data. More generally,

$$\delta_x \approx \frac{\lambda}{2(\sin\theta_{\rm tx}^{\max} + \sin\theta_{\rm rx}^{\max})}. \tag{15}$$

Here, $\theta_{\rm tx}^{\max}$ and $\theta_{\rm rx}^{\max}$ are determined by the size of the acquisition aperture, see Eq. (12) or by the antenna beamwidths, whichever is less. It is clear that wide-beamwidth antennas (e.g., omnidirectional antennas) are preferable as they provide wider viewing angles of the imaged object thereby improving the spatial resolution. Also, we recognize that larger values of $\theta_{\rm tx}^{\max}$ and $\theta_{\rm rx}^{\max}$ imply longer signal paths in the planar acquisition considered here. In a lossy propagation medium, this means loss of information at larger angles, which would degrade the resolution performance additionally.

2.1.2. Double-source Illumination

In the case of double-source illumination, the scattered signal due to a point scatterer in the differential case is approximated as

$$S^{-}_{0,\mathrm{d}}(x) \approx S^{-}_{\mathrm{da}}(x) = \left(e^{-jkR_{\mathrm{tx1}}} - e^{-jkR_{\mathrm{tx2}}}\right) e^{-jkR_{\mathrm{rx}}}, \tag{16}$$

whereas in the in-phase case, it is

$$S^{+}_{0,\mathrm{d}}(x) \approx S^{+}_{\mathrm{da}}(x) = \left(e^{-jkR_{\mathrm{tx1}}} + e^{-jkR_{\mathrm{tx2}}}\right) e^{-jkR_{\mathrm{rx}}}. \tag{17}$$

Here, R_{tx1} and R_{tx2} are the distances from sources 1 and 2 to the scatterer, respectively (see Fig. 2). If the angle defined by the vectors $\mathbf{R}_{\mathrm{tx1}}$ and $\mathbf{R}_{\mathrm{tx2}}$ (i.e., the angle supported by the double source when the vertex is at the scatterer's center) is sufficiently small, then

$$\begin{aligned} R_{\mathrm{tx1}} &\approx R_{\mathrm{tx}} + 0.5s \cdot \sin\theta_{\mathrm{tx}}, \\ R_{\mathrm{tx2}} &\approx R_{\mathrm{tx}} - 0.5s \cdot \sin\theta_{\mathrm{tx}}. \end{aligned} \tag{18}$$

This condition is fulfilled in the far zone of the double-source array or when θ_{tx} and θ_{rx} tend to 90°. Then, $S^{-}_{\mathrm{da}}(x)$ and $S^{+}_{\mathrm{da}}(x)$ can be written in terms of S_{a}, see Eq. (10), as

$$S^{-}_{\mathrm{da}}(x) = S_{\mathrm{a}}(x) \cdot 2j \sin\left(0.5ks \sin\theta_{\mathrm{tx}}\right). \tag{19}$$

Analogously, from Eq. (17) we get

$$S^{+}_{\mathrm{da}}(x) = S_{\mathrm{a}}(x) \cdot 2\cos\left(0.5ks \sin\theta_{\mathrm{tx}}\right). \tag{20}$$

The argument $0.5ks \sin\theta_{\mathrm{tx}}$ can also be written as

$$\frac{ks}{2} \sin\theta_{\mathrm{tx}} = \frac{ks}{2R_{\mathrm{tx}}} \cdot x. \tag{21}$$

This result indicates an increase in the spectral content of $\tilde{S}^{-}_{\mathrm{da}}$ and $\tilde{S}^{+}_{\mathrm{da}}$ as compared to $\tilde{S}_{\mathrm{a}}$ by $ks/(2R_{\mathrm{tx}})$. This increase would be insignificant if $R_{\mathrm{tx}} \gg s$. However, in near-field imaging, where $R_{\mathrm{tx}} \approx s$, the spectral width would double. Note that the highest spectral components in the system PSF arise when the receiver/transmitter pair is at the edge of the acquisition aperture, in which case the approximations in Eq. (18) hold in the near zone as well.

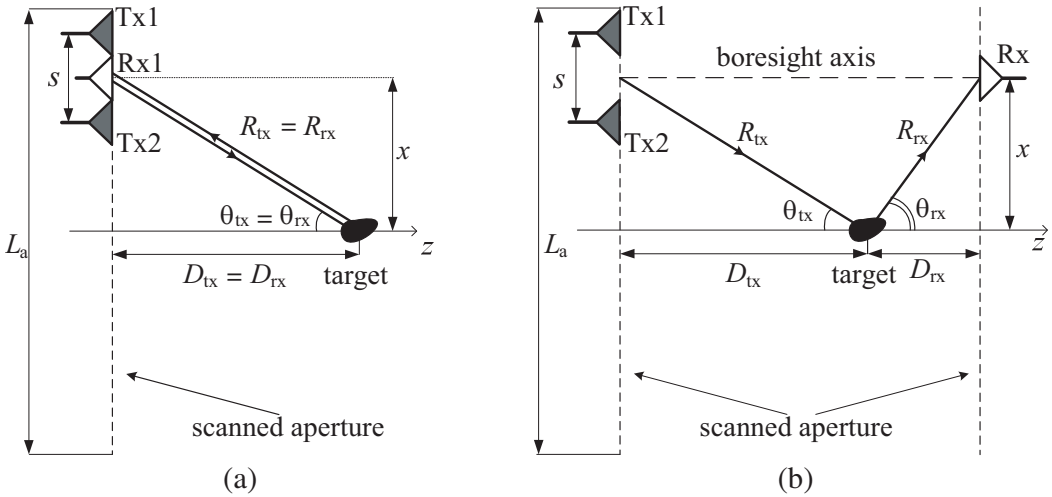

Figure 2. Illustration of the antenna and target positions in planar raster scanning in the case of differential illumination: (a) monostatic, (b) bi-static.

To appreciate this effect in real (x) space, we can write explicitly the derivatives of the differential and the in-phase PSFs as

$$\frac{dS_{\mathrm{da}}^{-}}{dx} = -jk(\sin\theta_{\mathrm{tx}} + \sin\theta_{\mathrm{rx}})S_{\mathrm{da}}^{-} + j\frac{ks}{D_{\mathrm{tx}}}\cos\left(\frac{ks}{2}\sin\theta_{\mathrm{tx}}\right)\cdot\cos^3\theta_{\mathrm{tx}}\cdot S_a \tag{22}$$

and

$$\frac{dS_{\mathrm{da}}^{+}}{dx} = -jk(\sin\theta_{\mathrm{tx}} + \sin\theta_{\mathrm{rx}})S_{\mathrm{da}}^{+} - \frac{ks}{D_{\mathrm{tx}}}\sin\left(\frac{ks}{2}\sin\theta_{\mathrm{tx}}\right)\cdot\cos^3\theta_{\mathrm{tx}}\cdot S_{\mathrm{a}}. \tag{23}$$

In the right-hand sides of Eqs. (22) and (23), the first terms indicate the presence of high spectral components due to signals at the aperture's edge such that $|k_x^{\max}| \approx k(\sin\theta_{\mathrm{tx}}^{\max} + \sin\theta_{\mathrm{rx}}^{\max})$. This is a result equivalent to the case of the single-source illumination considered above. On the other hand, when $\theta_{\mathrm{tx}}, \theta_{\mathrm{rx}} \to 0^\circ$ the response sensitivity with the single-source illumination is zero as per Eq. (11), i.e., the response is insensitive to variations in the cross-range position of the target. This is also the case with the in-phase double-source illumination, i.e., $dS_{\mathrm{da}}^{+}/dx \to 0$ for $x \to 0$. However, the signal sensitivity with the differential illumination remains nonzero:

$$\left.\frac{dS_{\mathrm{da}}^{-}}{dx}\right|_{\theta_{\mathrm{tx}},\theta_{\mathrm{rx}}\to 0} \approx j\frac{ks}{D_{\mathrm{tx}}}\cdot S_{\mathrm{a}}(x=0). \tag{24}$$

In summary, the cross-range resolution can be improved by at least a factor of 2 in near-field imaging by using double-source illumination such that the element separation is comparable to the range distance. The improvement is due to the introduction of incident field patterns that vary spatially faster than the one obtained with a single source. The effect can be further enhanced by using arrays consisting of more than 2 elements. This finding is particularly important in the imaging of lossy objects often encountered in non-destructive testing and medical (tissue) imaging. In this case, near-field data acquisition is a necessity since the signals attenuate fast and must be captured close to the abnormalities that generate them. Moreover, the angles $\theta_{\mathrm{tx}}^{\max}$ and $\theta_{\mathrm{rx}}^{\max}$ are severely limited by the attenuation associated with longer signal paths. Thus, it is important to have high signal sensitivity to target positions centered on and around the aperture's axis, which is not the case with the single-source illumination. In this respect, an optimal choice is the differential (or the ANI) array configuration. The ANI configuration offers the added and very important advantage of eliminating the need to acquire the baseline (or reference) system response as this response is simply zero (or nearly so).

2.2. Range Resolution

It is well known that the range resolution limit with far-zone measurements is given by [24]

$$\delta_z \approx \frac{c}{2B}. \tag{25}$$

Here, $B = (\omega_{\max} - \omega_{\min})/2\pi$ is the signal bandwidth.

It is clear that the range resolution depends primarily on the frequency bandwidth. Therefore, the double-source illumination is not expected to bring substantial improvement in this regard. This can also be understood by considering the signal sensitivity with respect to variations in the range position of a target. The double-source illumination introduces a rapidly-varying incident field in the lateral direction thus improving the cross-range resolution. However, it does not change significantly the field's behavior along range in comparison with the conventional illumination. We briefly note that the range resolution could be improved by introducing 3D illuminating arrays or multiple planes of acquisition along range. This problem's solution is not pursued here.

3. BACKGROUND DE-EMBEDDING

Figure 3(a) shows a simple example of the conventional illumination scheme. Two antennas, aligned along each other's boresight, form a two-port network together with the imaged volume. Each antenna may operate as a transmitter (Tx) and as a receiver (Rx) thus allowing for the acquisition of two

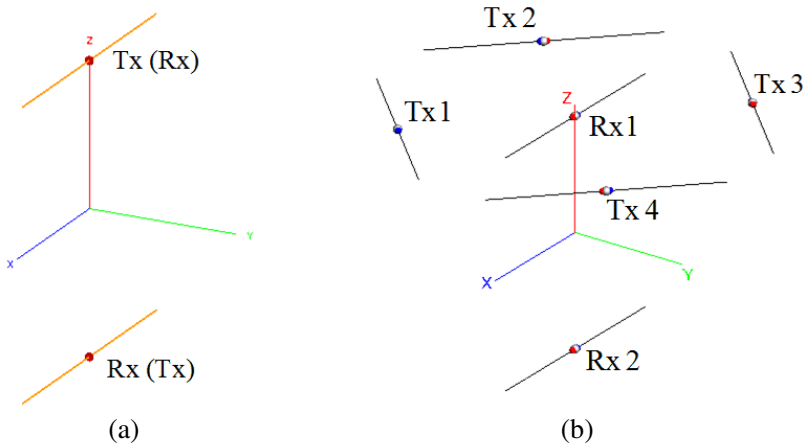

Figure 3. (a) Conventional measurement setup consisting of two half-wavelength dipoles along with (b) a transmitting ANI arrangement of dipoles (Tx1 to Tx4) together with two receiving antennas (Rx1 and Rx2) centered on the ANI central axis.

reflection and two transmission coefficients. This configuration can be expanded into an electronically-switched array or can be scanned mechanically. Often, both electronic switching and mechanical scanning are employed since the spatial sampling rate of electronically-switched arrays may not be sufficient.

In both transmission and reflection measurements, the single-source illumination scheme results in relatively strong received signals even when the scatterer-free background is measured. These signals are referred to as the *baseline* signals, which are representative of the incident-field component in the scattering equations. The baseline signals are clearly significant with forward measurements since in this scenario, the transmitter and at least one sensor are aligned along each other's boresight while operating without any obstruction. The baseline reflected signals may also be strong relative to the reflection from a weak scatterer since achieving a perfect impedance match of the antenna is difficult, especially in a wide frequency range.

In view of the above, it is clear that when an object under test (OUT) is examined, the acquired signal S_{OUT} contains two components: one due to the baseline signal, which can be interpreted as the incident-field signal component, and one due to the signal scattered from the OUT, which can be interpreted as the scattered-field component. We are interested in the scattered-field component S_{sc} as it carries information about the target.

The baseline signal S_{RO} is acquired with a measurement in the background medium, here referred to as the *reference object* (RO). The acquisition of S_{RO} is part of the system calibration and is, in principle, independent of any subsequent OUT measurements. Then, the baseline signal S_{RO} is subtracted from S_{OUT} to obtain an estimate of S_{sc}, $S_{\mathrm{sc}} = S_{\mathrm{OUT}} - S_{\mathrm{RO}}$. This simple approach to background de-embedding is based on the assumption that the mutual coupling between the acquisition hardware and the target can be neglected and the OUT signal is simply a superposition of the baseline and the scattered signals.

Two main problems ensue due to the need to estimate the baseline signal S_{RO}. First, the respective calibration measurements are needed — often performed before each OUT measurement. Second, the baseline signal contains systematic and stochastic noise and uncertainties at levels comparable to those contained in S_{OUT}. Provided the baseline measurement is performed under exactly the same circumstances as those of the OUT — a challenging requirement on its own — the systematic errors should cancel. Unfortunately, stochastic noise and uncertainties in the positioning do not cancel.

To address the above problems, here we propose a new axial-null illumination (ANI) scheme (Fig. 3(b)). The ANI can be viewed as the 2D extension of the differential illumination discussed above. It is inspired by the same illumination concept used in optical lithography for improving the spatial resolution [25, 26]. An alternative term, "off-axis illumination" (OAI), is also used in the optical literature. In principle, ANI can be used in planar, cylindrical and spherical scanners, although in this

work, we focus on its application with planar scanning.

Since ANI is a multi-source illumination, it has an enhanced cross-range resolution in near-field measurements as proved above. However, an additional advantage of such illumination is in reducing the noise and uncertainty in the data by decreasing significantly the strength of the baseline signals. Ideally, these signals should be zero due to the intrinsic antisymmetry of the illumination. In practice, they are suppressed down to the noise floor of the receiver or the measurement uncertainties. Most importantly, near-zero baseline signals allow to forego the calibration measurements in the background medium.

It should be noted that due to a null along the central axis, ANI may be viewed as somewhat similar to null steering antennas (NSA) used in the wireless communications industry [27, 28]. GPS systems, for example, are vulnerable to electromagnetic jamming because of the wide angular coverage. By reconfiguring the radiation pattern, NSA can generate a null in a given direction where the interference source is located. However, steering of the radiation pattern null is not needed in microwave imaging. Also, ANI has only one fixed null along its central axis for the purpose of having near-zero baseline signals as well as the large gradient of the incident field, which makes it different from the NSA applications.

4. ANI: SETUP AND DESIGN REQUIREMENTS

A simulation example of an ANI transmitting arrangement using FEKO [29] is illustrated in Fig. 3(b). This particular configuration consists of 4 transmitting and 2 receiving dipoles. Both receiving antennas are centered on the axis of the ANI. The dipole Rx1 is used to acquire back-scattered signals whereas the antenna along the ANI axis but on the opposite side of the imaged volume (Rx2) acquires the forward-scattered signals.

The goal of ANI, as explained earlier, is to ensure zero baseline signals, i.e., zero field along the ANI's axis, in a background medium that is uniform or layered. Depending on the antenna elements, there are at least two planar arrangements that can achieve this goal. These are illustrated in Fig. 4 where dipoles are used. These two arrangements have the same geometry, i.e., the dipoles' spacing and orientations are the same, but their phasing differs. The first arrangement (in Fig. 4(a)) features 2 mutually orthogonal planes of antisymmetry intersecting at the ANI's center. The second one (shown in Fig. 4(b)) has two pairs of such planes of antisymmetry.

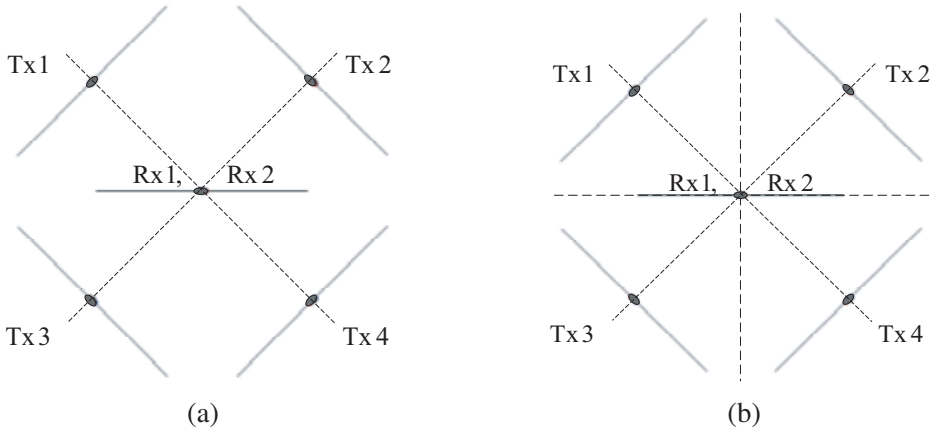

Figure 4. Top view of the two cases of the ANI design with dipoles: (a) with 2 antisymmetry planes, and (b) with 4 antisymmetry planes. The planes of antisymmetry are shown with dash lines.

The proposed illumination scheme may appear counter-intuitive as it is clear that if a target is located along the ANI's axis, it is not going to be detected — it is not illuminated, therefore, it does not scatter. However, ANI creates an illumination interference pattern (see Fig. 5). While a null of this pattern lies at its center, maxima reside nearby. Depending on the separation between the ANI elements, the distance to the target and the wavelength, the field maxima can be anywhere between one

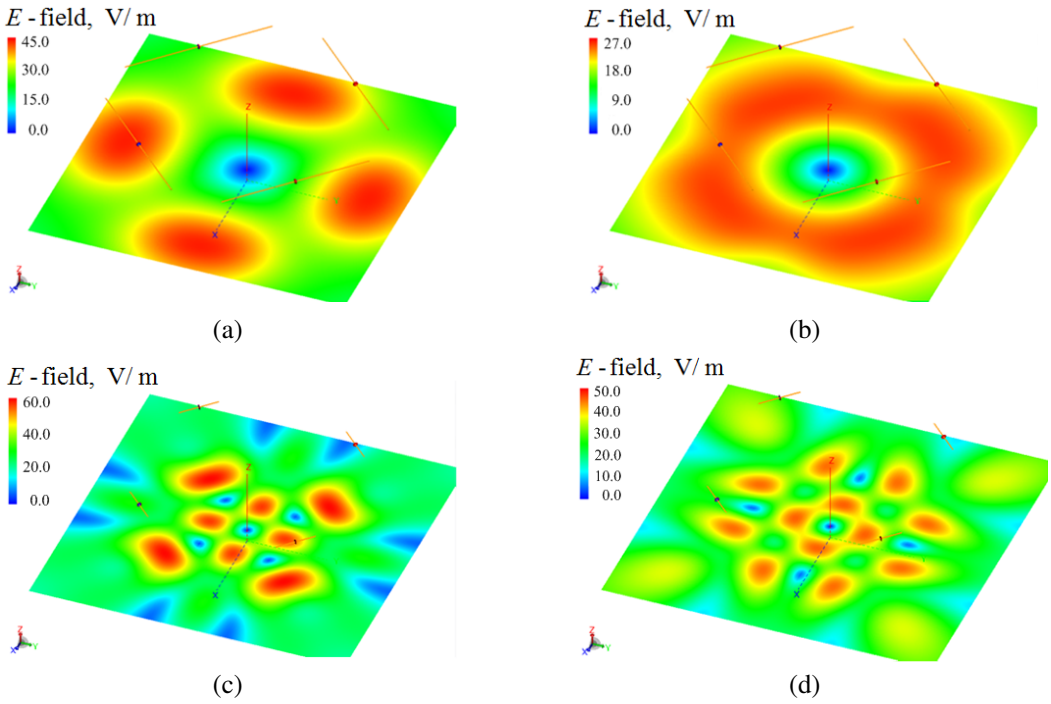

Figure 5. Screenshot from a FEKO simulation showing the E-field strength in a plane intersecting the RO (background medium) at a distance of 20 mm from the plane of the ANI in the case of the configuration in: (a) Fig. 5(a) (2 antisymmetry planes) at 3 GHz; (b) Fig. 5(b) (4 antisymmetry planes) at 3 GHz; (c) Fig. 5(a) (2 antisymmetry planes) at 11 GHz; (d) Fig. 5(b) (4 antisymmetry planes) at 11 GHz. The separation between the ANI elements is 70 mm.

and two times stronger than the boresight maximum created by a single element provided comparable power is fed to each of the ANI array elements. If the interference pattern changes sufficiently fast in space, even a slight displacement of a target from the center disturbs the field antisymmetry and results in a non-zero received signal. This signal is a purely scattered signal, i.e., ideally, it does not have an incident-field component ($S_{\mathrm{RO}} = 0$).

The design of the ANI array depends on the choice of its antenna elements. With the antenna elements known, the design involves choosing the separation distance between them as well as determining their orientation, which is dependent mostly on the antenna polarization. The ANI array can be optimized for best sensitivity by requiring that: (i) the field along the central axis (the z axis in Fig. 3) is zero; (ii) within the square area defined by the centers of the ANI elements, there are at least four maxima of the interference pattern. The latter requirement ensures that the strength of the scattered signal is no less than that in conventional illumination since the signal path from a maximum of the interference pattern to the receiving antenna is not much longer compared to the signal path along the boresight axis. It also ensures large field gradient at the ANI array axis leading to high sensitivity to the position of the scatterer.

We approach the problem of choosing the optimal separation of the ANI elements by considering the simpler 2D differential arrangement, which consists of two out-of-phase transmitters. This arrangement is shown in Fig. 6, where d is the focusing distance, i.e., the distance between the line of the transmitters (Tx1 and Tx2) and the line of the imaged points. The two lines are parallel. In Fig. 6, x_o is the observation point, s is the separation between the two elements, R_i ($i = 1, 2$) is the distance between the i-th transmitter and the observation point. To obtain an analytical estimate, the problem is further simplified by assuming point sources. The point sources approximation (also known as isotropic source approximation) is commonly exploited in far-field estimations and analyses of antenna arrays since the results can be easily augmented to represent realistic antennas via a simple multiplication with the antenna pattern. Therefore, the point-source simplification is valid as long as the focusing plane is not

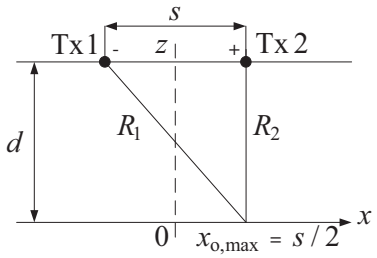

Figure 6. The differential illumination as a 2D ANI version.

in the reactive near field of the antenna element.

For the case illustrated in Fig. 6, the field at the observation point x_o can be written as the superposition

$$E_x^{\text{inc}}(x_o) \propto e^{-jkR_1} - e^{-jkR_2}, \tag{26}$$

where k is the wavenumber of the background medium. Note that when the background medium is lossy, it can be properly accounted for in the expression for k. A maximum of the interference pattern is required at $x_o \leq s/2$ at the lowest frequency (or the largest wavelength $\lambda_{\max}$). The distances from Tx1 and Tx2 to $x_{o,\max} = s/2$ are

$$R_1 = \sqrt{d^2 + s^2} \quad \text{and} \quad R_2 = d. \tag{27}$$

The constructive interference occurs when

$$kR_2 = kR_1 + \pi(2n+1), n = 0, 1, \ldots, \tag{28}$$

where $n = 0$ corresponds to the first maximum. Therefore, with $n = 0$, the equation for a maximum at $x_{o,\max} = s/2$ is

$$\sqrt{\bar{d}^2 + \bar{s}^2} - \bar{d} = 0.5, \tag{29}$$

where $\bar{d} = d/\lambda_{\max}$, $\bar{s} = s/\lambda_{\max}$. The relation between $\bar{s}$ and $\bar{d}$ can then be found as

$$\bar{d} = \bar{s}^2 - 0.25, \bar{s} > 0.5 \quad \text{or} \quad s > \frac{\lambda_{\max}}{2}. \tag{30}$$

The requirements for dense sampling and large gradient of the incident-field distribution demand as small separation $\bar{s}$ as possible. On the other hand, the separation is limited from below by the size of the ANI elements and the need to minimize mutual coupling. Thus, the requirement $s \geq \lambda_{\max}/2$ is usually met in practice. Conversely, if a specific focusing distance d is required (typically centered in the middle of the imaged volume), then s can be determined using (30). Note that the choice of $\bar{s}$ and $\bar{d}$ has implications for the spatial resolution as well. These were discussed in the previous section.

Figure 7 illustrates the field distribution at 3 GHz obtained analytically using (26). The longest wavelength (in air) is $\lambda_{\max} \approx 100$ mm. The separation is set at $s = 70$ mm. Three distributions are shown corresponding to $d = 15$ mm, 24 mm and 35 mm. According to (30), at $d_0 = 24$ mm, the field-strength peaks are aligned with the separation s. This is indeed the case as is evident from Fig. 7. For $d < d_0$, the peaks shift inward within the interval defined by s, which is a desirable effect. For $d > d_0$ they move out of s, which is not desirable. In summary, for maximum sensitivity, the focusing distance d has to be kept smaller than or approximately equal to d_0, where d_0 is determined according to (30).

In the case of far-zone measurements, i.e., $\bar{d} > \bar{s}$ ($\bar{d} > 1, \bar{s} > 1$), it can be shown that the same requirement leads to $\bar{s}^2 \approx \bar{d}$. We note that this requirement ensures the maximum possible field gradient at the axis of the ANI and therefore the maximum sensitivity. However, even if the above conditions are not met, the benefits of zero on-axis incident field remain.

5. VALIDATION IN DIRECT QUANTITATIVE RECONSTRUCTION

The validation of the expected improvement due to the ANI is carried out with the SPM direct imaging method proposed in [22]. Since the method does not need analytical or numerical approximations

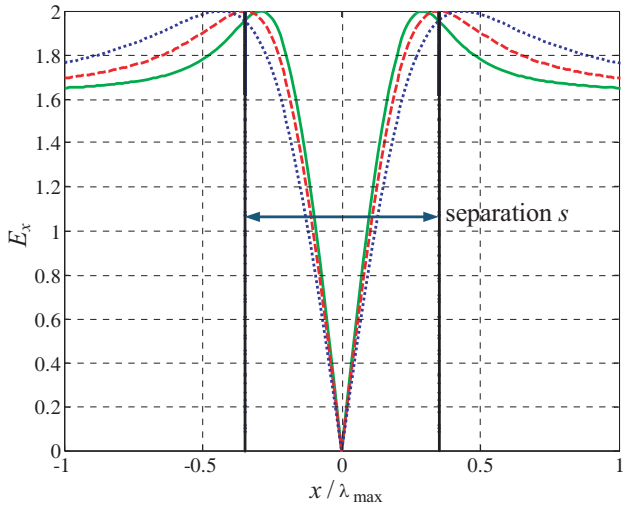

Figure 7. Magnitude distribution of the incident field for three different values of the distance d to the observation plane: $d = 15\,\text{mm}$ (solid), $24\,\text{mm}$ (dash) and $35\,\text{mm}$ (dot) in the case of differential illumination at $3\,\text{GHz}$. The separation $s = 70\,\text{mm}$.

of the forward model, it is particularly beneficial in near-field imaging. The electrical properties of the imaged objects are reconstructed using a resolvent kernel in the forward model which is extracted from calibration measurements. These measurements are performed on two known objects: an RO representing the background medium and a calibration object (CO) formed by an electrically small scatterer embedded in the RO. The size of the electrically small scatterer must be below $\lambda/4$, where λ is the shortest wavelength inside the small scatterer or that in the RO, whichever is shorter. Since the CO response provides the resolvent kernel in SPM, the rule of thumb is that if the CO cannot be reconstructed, the OUT reconstruction would not be successful either. Therefore, it is important to ensure that the CO scattered signal is detectable by the imaging system, i.e., it is well above the noise floor and the measurement uncertainties. In some challenging scenarios and particularly in biomedical imaging, the raw data can be significantly corrupted by attenuation, noise, and positioning uncertainties, which may hinder the successful detection of the point scatterer. In such cases, it is recommended to enlarge the scatterer size and/or the contrast. On the other hand, the small scatterer in the CO should be small enough to feature an approximately uniform internal field distribution which is assumed in the forward model of SPM [22]. If the scatterer is not electrically small and its response is a summation of point scatterers, the acquired response is not a system point-spread function and the reconstruction is likely to fail. Also, the permittivity of the small scatterer in the CO should be close to that of the OUT in order to get the most accurate quantitative results. However, good qualitative reconstruction is attainable with any permittivity of the small scatterer as long as multiple scattering is negligible. These considerations regarding the size and permittivity of the small scatterer serve as guidelines when choosing the CO.

Note that since SPM is a direct inversion method, it is incapable of taking into account mutual coupling effects as well as the multiple scattering in the OUT. Therefore, it is limited to the weak-scattering problems.

5.1. Cross-Range Resolution Study

To investigate the resolution limits for both the conventional and axial-null illuminations, we simulate an OUT consisting of 2 dielectric cubes of $5\,\text{mm}^3$ volume with relative permittivity of $\varepsilon_{\text{OUT}} = 1.2 - i0.0$ (Fig. 8). The RO is chosen to be air, while the CO has a small dielectric cube of $5\,\text{mm}^3$ volume with relative permittivity of $\varepsilon_{\text{CO}} = 1.1 - i0$, placed in the center of the imaged plane. Note that the RO data have been used for reconstruction only in the conventional illumination case.

The ANI array has a separation $s = 70\,\text{mm}$. The distance between the transmitting and receiving

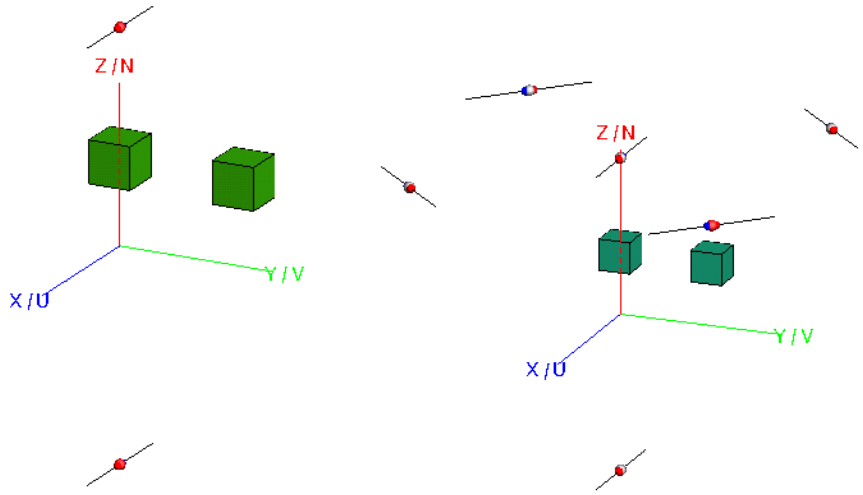

(a) (b)

Figure 8. Illumination setup in FEKO for the imaging of 2 dielectric cubes in the cross-range (xy) plane: (a) conventional case and (b) ANI case.

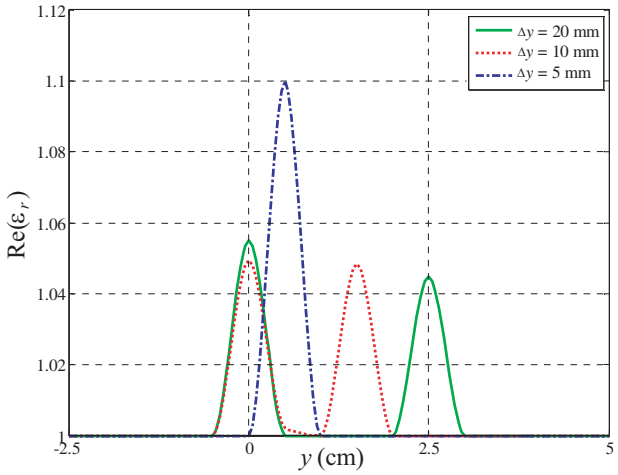

Figure 9. Real part of the reconstructed relative permittivity of the two cubes along the y axis at 8 GHz for the conventional illumination case. The edge-to-edge distances between the cubes are: 20 mm (solid), 10 mm (dot) and 5 mm (dash-dot).

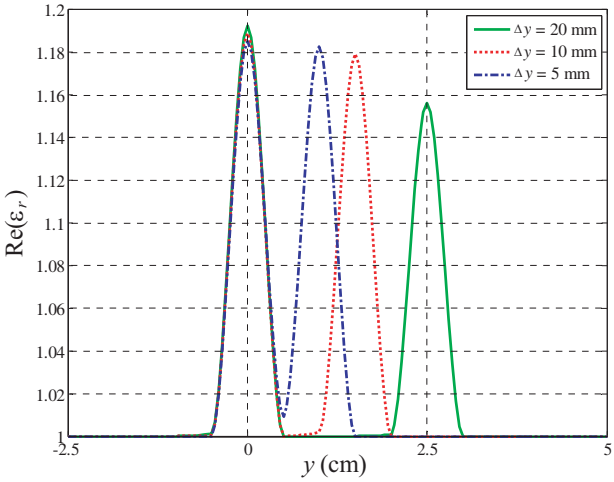

Figure 10. Real part of the reconstructed relative permittivity of the two cubes along the y axis at 7 GHz for the ANI case. The edge-to-edge distances between the cubes are: 20 mm (solid), 10 mm (dot) and 5 mm (dash-dot).

planes is 50 mm. The focusing distance from the transmitters to the middle of imaged objects is 15 mm. In both illumination schemes, the transmitters and the receivers are half-wavelength dipoles (the physical length is adjusted at each frequency) at frequencies from 5 GHz to 9 GHz.

To investigate the cross-range resolution, three cases are considered: dielectric cubes at edge-to-edge distances of $\Delta y = 20$ mm, 10 mm and 5 mm (Fig. 8).

Figure 9 shows a cut of the reconstructed relative permittivity of two dielectric cubes along the y axis in the case of conventional illumination. It is evident that at 8 GHz the two objects merge into one when the edge-to-edge distance is 5 mm. Thus, the estimated resolution limit is about $\lambda/4$, where $\lambda = 37.5$ mm is the free-space wavelength at 8 GHz. This result is in agreement with the estimated cross-range resolution in the conventional illumination case given in Eq. (14).

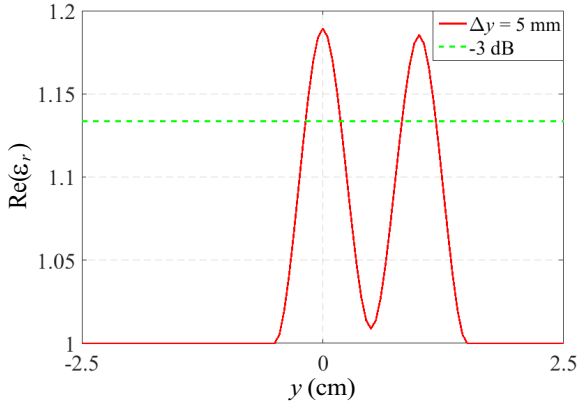

Figure 11. Real part of the reconstructed relative permittivity of the two cubes along the y axis at 5.7 GHz for the ANI case (red solid) and -3 dB level (green dashed). The edge-to-edge distance between the cubes is 5 mm (center-to-center distance is 10 mm).

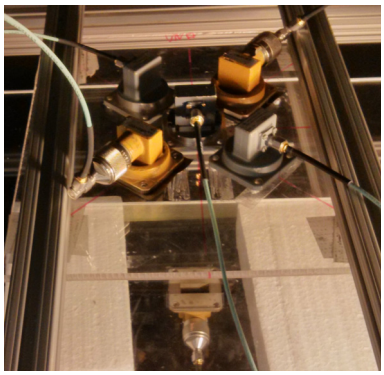

Figure 12. ANI array consisting of four transmitting X-band open-end waveguides (at the top plane) plus a conventional single-source illumination element at the center. Receiver is located at the bottom.

In the case of ANI, the reconstructed relative permittivities of the imaged cubes at 7 GHz are shown in Fig. 10. In all three cases, it is possible to differentiate the two objects. Fig. 11 shows that in the case of ANI and when $\Delta y = 5$ mm, the two objects can still be distinguished well at 5.7 GHz. Therefore, the estimated cross-range resolution is approximately $\lambda/10$, where $\lambda = 52.6$ mm is the free-space wavelength at 5.7 GHz. This result is in agreement with the theory presented above where it has been shown that the cross-range resolution for the ANI case can be improved by at least a factor of 2 in comparison with the conventional illumination.

5.2. Experimental Example 1

The experimental setup consists of five identical open-end waveguides at the top and one at the bottom as shown in Fig. 12. The four waveguides at the corners of the top array realize an ANI, whereas the central waveguide serves as a conventional single-source illumination element. The waveguide at the bottom serves as a receiver only. We acquire only forward-scattered signals with both illumination schemes. The ANI elements are connected to separate vector network analyzer ports and the respective transmission coefficients to the receiving open waveguide at the bottom plane are acquired. These transmission coefficients are added to produce a total response that emulates simultaneous illumination. Note that the four elements of the ANI array are oriented so that this total response is near zero in the baseline measurement; in practice, it varies from -60 dB to -53 dB across the X-band range.

The ANI array has a separation of 95 mm and the focusing distance equals 50 mm as calculated from (30) for the 8 GHz frequency. The presented illumination structure in Fig. 12 is part of the planar-raster acquisition system. The imaged area is 20 cm by 20 cm. The sampling step in both lateral directions is 5 mm [30].

The imaged dielectric cylinders of 1 cm height and 1 cm diameter have complex relative permittivity of $\varepsilon_{\mathrm{OUT}} = \varepsilon'_{\mathrm{OUT}} - i\varepsilon''_{\mathrm{OUT}} = 50 - i0$ (Fig. 13). The CO used consists of air with a dielectric cylinder identical to those in OUT, placed in the center of the imaged plane. The cylinder represents a point scatterer and its size determines the expected imaging resolution [22].

The reconstructed OUT using the SPM with the conventional illumination and ANI is shown in Fig. 14. Notice that the RO data have not been used in neither of the reconstructions. It is observed that the quality of the reconstructed images in the ANI case is much better since the detrimental effect of the baseline signal is minimized by ANI. On the contrary, Fig. 14(a) demonstrates the conventional-case scenario where the reconstructed image is obtained from the OUT data being a superposition of the baseline and scattered signals. We emphasize that the same reconstruction method is used in

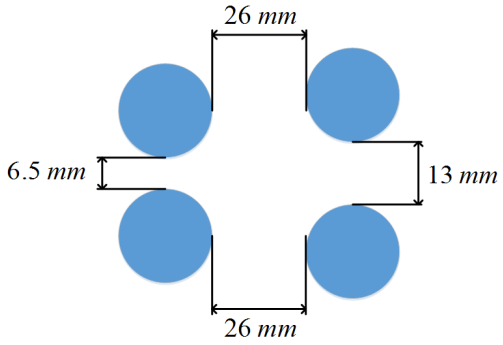

Figure 13. Schematic view of four identical dielectric cylinders serving as OUT. The separation distances are chosen approximately equal to $\lambda_0/4$, $\lambda_0/2$ and λ_0 at the central frequency of the X-band.

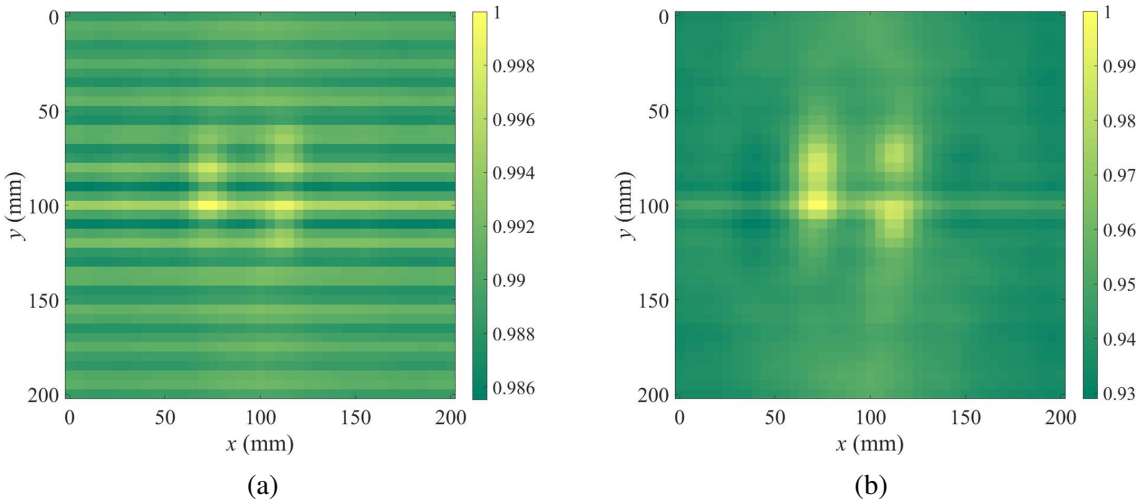

Figure 14. Qualitative reconstruction results of four dielectric cylinders for the frequency sweep from 8 GHz to 12 GHz: (a) with conventional illumination and (b) with ANI. Transmission coefficients only are processed in this example. The results are normalized to 1.

generating both images in Fig. 14. The improvement observed in Fig. 14(b) is entirely due to the proposed axial-null illumination scheme.

As a final observation, we note that the dynamic range of the reconstructed images is larger in the ANI case compared to that in the conventional illumination case (Fig. 14).

5.3. Experimental Example 2

For the second example, we attempt to image objects behind drywall with the ANI and with conventional illumination. Photos of the OUT and some of its components are shown in Fig. 15. The OUT consists of a piece of drywall of size 47 cm by 36 cm by 1.3 cm, a drywood stud of size 47 cm by 8.8 cm by 3.7 cm and a plastic water pipe of 1.6 cm diameter together with an insulated three-wire electric cable. Since the dielectric permittivity of the drywall is relatively small ($\varepsilon_r \approx 2.2$, $\tan\delta \approx 0.01$ as per [31]), we use the same experimental setup consisting of X-band air-filled waveguides as in the previous experiment (see Fig. 12). However, this time we are interested in the reflection measurements only since such scenarios admit only single-side access. Thus, the receiver at the bottom has been removed. In the case of ANI, the central element of the top array transmits with the respective four transmission coefficients acquired. We use a 4-port test set allowing for a multi-port acquisition. It has been observed that this 4-port test set carries a considerable amount of attenuation, on the order of 5 dB to 10 dB depending

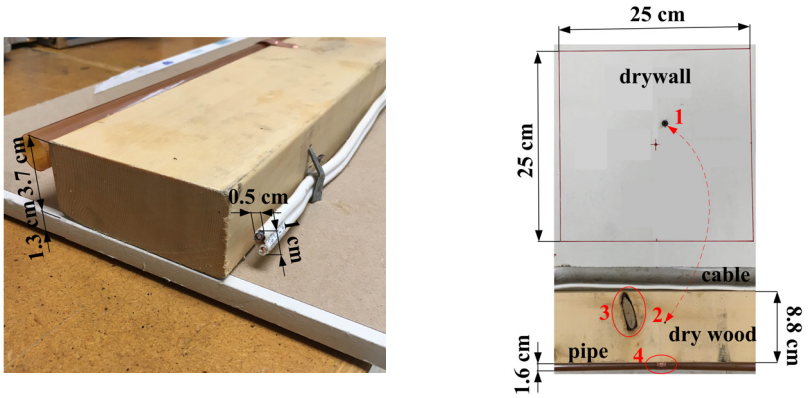

Figure 15. The OUT consisting of drywall of size 47 cm by 36 cm by 1.3 cm, a piece of dry-wood stud of size 47 cm by 8.8 cm by 3.7 cm, a water pipe of 1.6 cm in diameter attached to the left side of the stud, and a three-wire electric cable attached to the right side of the stud: (a) the isometric view of the whole OUT upside down and (b) the top view of the disassembled OUT (part to be imaged is shown only). The imaged area is shown with a red square. The correspondence between the screw 1 and its hole 2 in the dry wood is shown with the red dashed arrow. The wood knot is shown as object 3 whereas the metallic brace attaching the pipe to dry wood is shown as object 4.

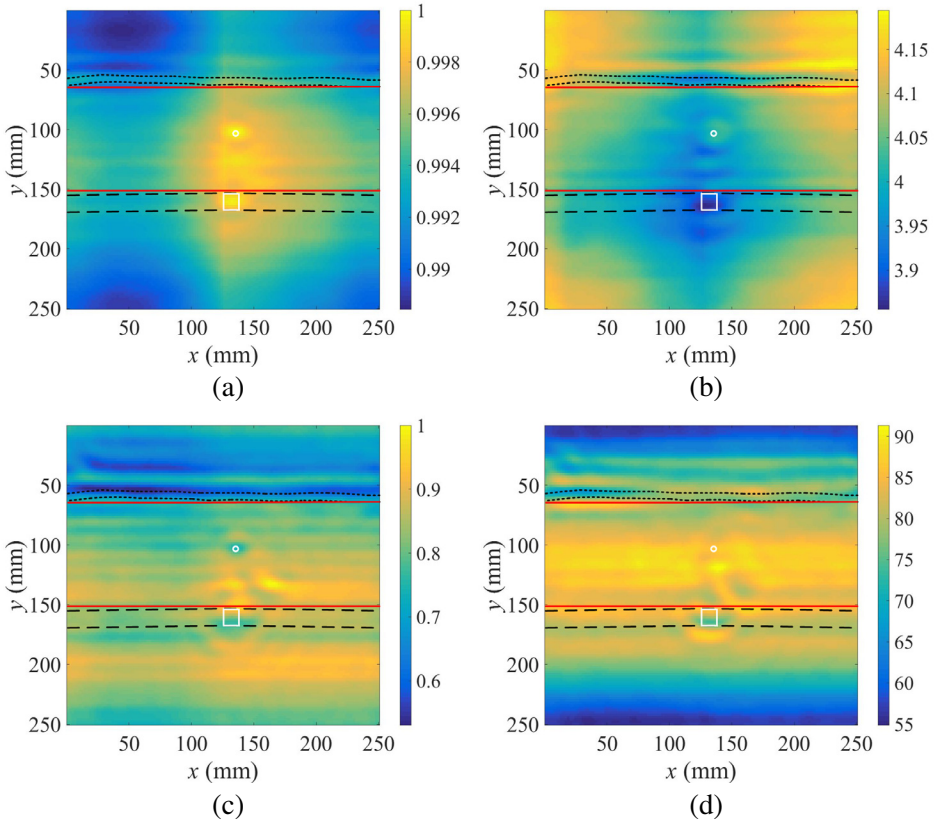

Figure 16. Qualitative reconstruction results for the second experiment: with conventional illumination (a) normalized magnitude and (b) phase in degrees, and with ANI (c) normalized magnitude and (d) phase in degrees. The frequency sweep is from 8 GHz to 12 GHz. The contour lines of the cable are dot black, the contour lines of the dry wood are solid red, the contour lines of the pipe are dashed black, and the contour lines of metallic objects are solid white (a circle and a square).

on frequency. In order to ensure that the measurements with ANI setup are reasonable, we include amplification to counteract the loss of power.

Since we aim at qualitative reconstruction, the CO is chosen to be a metallic cylinder attached to the bottom of the drywall and placed at the center of the imaged plane. The cylinder is 1 cm in height and 1 cm in diameter.

In the conventional illumination case, only the reflection coefficient at the central element of the array is acquired (Fig. 12). Therefore, the 4-port test set is not used in this case. Also, since it is a reflection measurement, an amplifier cannot be used. Ultimately, the output power is -2 dBm in the conventional illumination case whereas the output power in the ANI case is 14 dBm.

The ANI array has a separation of 95 mm and the focusing distance is 5 mm which is in agreement with Eq. (30) for the 8 GHz frequency. The planar-raster acquisition system is used with the imaged area being 25 cm by 25 cm. The sampling step in both lateral directions is 2 mm.

Using the SPM, the imaged OUT in the conventional illumination case and in the ANI case is shown in Fig. 16. We observe more detailed reconstruction with all the objects being distinguishable in the case of ANI. In the conventional illumination case, there is a significant artifact along the x and y axes. Also, the water pipe cannot be seen.

As in the previous example, the dynamic range of the images in the ANI case exceeds that in the conventional illumination case. However, this time such a significant difference in the dynamic ranges is explained by using an amplifier for the measurements with ANI.

6. CONCLUSION

Rigorous proof of the improvement in cross-range resolution in the multi-illumination case compared to the conventional single-source illumination is developed. Based on this, an optimized ANI scheme for near-field microwave imaging is proposed. Due to the intrinsic antisymmetry of such illumination, the baseline signals are suppressed down to the noise level of the measurement system. Therefore, the proposed axial-null illumination simplifies the calibration process by eliminating the need to acquire the responses in the scatterer-free background. On the other hand, the sharp gradient of the field magnitude within the separation distance provides high sensitivity to the position of a scatterer.

The discussed improvements are expected to occur not only for the direct SPM imaging method used here for validation purposes, but also for any other imaging technique that exploits wave-like physical fields. This is because the improvement results from the geometrical configuration of emitters and sensors as well as the fast-changing incident field distribution, and not the specifics of the reconstruction method.

The initial experimental results obtained with four X-band open-end waveguides demonstrate a better reconstruction quality in the ANI case over conventional single-source illumination provided that no RO data has been used. As the next step, we plan to undertake an extensive experimental study of ANI using the antennas introduced in [32].

Finally, we note that in principle, the field distribution with zero field at the center can be achieved at the step of processing the data coming from multiple sensors. In this way, there is no need for a complicated hardware while all the benefits of ANI can still be preserved.

REFERENCES

1. Nanzer, J., *Microwave and Millimeter-wave Remote Sensing for Security Applications*, Artech House, Norwood, MA, 2012.
2. Amin, M. G., *Through-the-Wall Radar Imaging*, CRC Press, Boca Raton, FL, 2011.
3. Zoughi, R., *Microwave Non-destructive Testing and Evaluation*, Kluwer Academic, Dordrecht, The Netherlands, 2000.
4. Vorst, A. V., A. Rosen, and Y. Kotsuka. *RF/Microwave Interaction with Biological Tissues*, Wiley, Hoboken, NJ, 2006.
5. Nikolova, N. K., "Microwave biomedical imaging," *Wiley Encyclopedia of Electrical and Electronics Engineering*, 1–22, published on-line Apr. 25, 2014.

6. Pastorino, M., *Microwave Imaging*, John Wiley & Sons, Hoboken, NJ, 2010.
7. Caorsi, S., G. L. Gragnani, and M. Pastorino, "An electromagnetic approach using a multi-illumination technique," *IEEE Trans. Biomed. Eng.*, Vol. 41, No. 4, 406–409, Apr. 1994.
8. Tseng, C.-H. and T.-H. Chu, "Improvement of quasi-monostatic frequency-swept microwave imaging of conducting objects using illumination diversity technique," *IEEE Trans. Antennas Propag.*, Vol. 53, No. 1, 305–312, Jan. 2005.
9. Helaoui, L., J. Bel Hadj Tahar, and F. Choubani, "Multi-source illumination approach for buried objects exploration," *2008 2nd Int. Conf. Dig. Soc.*, 146–149, Sainte Luce, Feb. 2008.
10. Zhao, Y., W. Shao, and G. Wang, "UWB microwave imaging for early breast cancer detection: Effect of two synthetic antenna array configurations," *2004 IEEE Int. Conf. Syst., Man and Cybern.*, Vol. 5, 4468–4473, Oct. 2004.
11. Meaney, P. M., M. W. Fanning, D. Li, S. P. Poplack, and K. D. Paulsen, "A clinical prototype for active microwave imaging of the breast," *IEEE Trans. on Microwave Theory and Tecnniques*, Vol. 48, No. 11, 1841–1853, Nov. 2000.
12. Zakaria, A., C. Gilmore, and J. LoVetri, "Finite-element contrast source inversion method for microwave imaging," *Inverse Problems*, Vol. 26, 115010, 2010.
13. Mojabi, P., M. Ostadrahimi, L. Shafai, and J. LoVetri, "Microwave tomography techniques and algorithms: A review," *Antenna Technology and Applied Electromagnetics (ANTEM)*, 1–4, Toulouse, France, Jun. 2012.
14. Semenov, S. Y., R. H. Svenson, A. E. Bulyshev, A. E. Souvorov, A. G. Nazarov, Y. E. Sizov, V. G. Posukh, A. V. Pavlovsky, P. N. Repin, and G. P. Tatsis, "Spatial resolution of microwave tomography for detection of myocardial ischemia and infarction — Experimental study on two-dimensional models," *IEEE Trans. on Microwave Theory and Tecnniques*, Vol. 48, No. 4, 538–544, Apr. 2000.
15. Gilmore, C., P. Mojabi, A. Zakaria, S. Pistorius, and J. LoVetri, "On super-resolution with an experimental microwave tomography system," *IEEE Antennas and Wireless Propag. Lett.*, Vol. 9, 393–396, 2010.
16. Klemm, M., I. J. Craddock, J. A. Leendertz, A. Preece, and R. Benjamin, "Radar-based breast cancer detection using a hemispherical antenna array — Experimental results," *IEEE Trans. Antennas Propag.*, Vol. 57, No. 6, 1692–1704, Jun. 2009.
17. Donelli, M., I. Craddock, D. Gibbins, and M. Sarafianou, "A three-dimensional time domain microwave imaging method for breast cancer detection based on an evolutionary algorithm," *Progress In Electromagnetics Research*, Vol. 18, 179–195, 2011.
18. Klemm, M., J. A. Leendertz, D. Gibbins, I. J. Craddock, A. Preece, and R. Benjamin, "Microwave radar-based breast cancer detection: Imaging in inhomogeneous breast phantoms," *IEEE Antennas and Wireless Propag. Lett.*, Vol. 8, 1349–1352, 2009.
19. Rocca, P., M. Donelli, G. L. Gragnani, and A. Massa, "Iterative multi-resolution retrieval of non-measurable equivalent currents for the imaging of dielectric objects," *Inverse Problems*, Vol. 25, No. 055004, 1–15, 2009.
20. Viani, F., M. Donelli, P. Rocca, R. Azaro, and A. Massa, "A multi-resolution three-dimensional approach based on SVM for breast cancer detection," *24th International Review of Progress in Applied Computational Electromagnetics*, 479–482, ACES, Niagara Falls, Canada, 2008.
21. Donelli, M., D. Franceschini, A. Massa, M. Pastorino, and A. Zanetti, "Multi-resolution iterative inversion of real inhomogeneous targets," *Inverse Problem*, Vol. 21, No. 6, S51–S63, 2005.
22. Tu, S., J. J. McCombe, D. S. Shumakov, and N. K. Nikolova, "Fast quantitative microwave imaging with resolvent kernel extracted from measurements," *Inverse Problems*, Vol. 31, No. 045007, 1–33, 2015.
23. Ravan, M., R. K. Amineh, and N. K. Nikolova, "Two-dimensional near-field microwave holography," *Inverse Problems*, Vol. 26, No. 5, 055011, May 2010.
24. Sheen, D. M., D. L. McMakin, and T. E. Hall, "Three-dimensional millimeter-wave imaging for concealed weapon detection," *IEEE Trans. on Microwave Theory and Techniques*, Vol. 49, No. 9,

Sep. 2001, 1581–1592.

25. Fritze, M., B. M. Tyrell, D. K. Astolfi, R. D. Lambert, D. W. Yost, A. R. Forte, S. G. Cann, and B. D. Wheeler, "Subwavelength optical lithography with phase-shift photomasks," *Lincoln Laboratory Journal*, Vol. 14, No. 2, 237–250, 2003.
26. Wong, A. K.-K., *Resolution Enhancement Techniques in Optical Lithography*, SPIE, Bellingham, WA, 2001.
27. Deng, C., Y. Li, Z. Zhang, and Z. Feng, "A hemispherical 3-D null steering antenna for circular polarization," *IEEE Antennas and Wireless Propag. Lett.*, Vol. 14, 803–806, 2015.
28. Sun, C., A. Hirata, T. Ohira, and N. C. Karmakar, "Fast beamforming of electronically steerable parasitic array radiator antennas: Theory and experiment," *IEEE Trans. Antennas Propag.*, Vol. 52, No. 7, 1819–1832, Jul. 2004.
29. FEKO Suite 6.3 EM Software & Systems, Inc., USA www.feko.info.
30. Shumakov, D. S., A. S. Beaverstone, D. Tajik, and N. K. Nikolova, "Experimental investigation of axial-null and axial-peak illumination schemes in microwave imaging," *IEEE AP-S/URSI Int. Symp. on Antennas and Propag.*, Fajardo, Puerto Rico, Jun. 2016.
31. Wilson, R., "Propagation losses through common building materials: 2.4 GHz vs. 5 GHz," E10589 Magis Networks, Inc., 1–27, Aug. 2002.
32. Jenks, C. H. J., "Dielectric pyramid antenna for GPR applications," *10th European Conf. on Antennas and Propag. (EuCAP)*, 1–3, Apr. 2016.